

# The role of flow interaction in flame-flame interaction events in a dual burner experiment

A. Tyagi<sup>1</sup>, I. Boxx<sup>2</sup>, S. Peluso<sup>1</sup>, J. O'Connor<sup>1\*</sup>

<sup>1</sup>*Mechanical and Nuclear Engineering, Pennsylvania State University, University Park, PA,*

*USA, 16802*

<sup>2</sup>*DLR, German Aerospace Center, Stuttgart, Germany, 70596*

\*Corresponding author

Address: 111 Research East Building, University Park, PA 16802

Email: [jxo22@engr.psu.edu](mailto:jxo22@engr.psu.edu)

Colloquium: Turbulent Flames

Alternate colloquium: Gas Turbine and Rocket Engine Combustion

Total length of paper: 6062

Method of determination: Method 1

We do not need a color print for the paper.

Main Text	3041
Figure 1	447
Figure 2	115
Figure 3	239
Figure 4	232
Figure 5	261
Figure 6	185
Figure 7	226
Table 1	68
Table 2	479
References	769
<b>TOTAL</b>	<b>6062</b>

## Abstract

A dual burner experiment is used to investigate how flow interactions affect local flame-flame interaction in turbulent premixed flames. The presence of adjacent flows influences the local structure of these flames and understanding the sensitivity of these flames to adjacent flows is essential for multi-nozzle combustion devices. To study this sensitivity, a high-aspect-ratio Bunsen flame operating at a constant flow velocity is placed adjacent to an identical burner with non-reacting flow at varying velocities. High-speed OH-planar laser induced fluorescence and stereoscopic-particle image velocimetry measurements are performed to capture flame-front locations and velocity fields. A non-rigid image registration technique is used to calculate the local flame-area variations that occur due to topological differences, and conditional statistics are extracted to relate the local behavior to changes observed in the global behavior of the flames. Extracted flame curvatures and time-averaged progress variables conditioned on flame-flame interactions show differences existing in the inner and outer flame branches near the flame-attachment region. Statistics of these results are presented and compared for all test cases.

**Keywords:** *Turbulent flames, Flame-flame interactions*

## 1 Introduction

Flame-flame interaction can strongly affect the structure and dynamics of turbulent flames in practical devices. Accurate and robust modelling of these devices therefore requires a detailed understanding of such interactions. Studies have shown that flame-flame interactions can cause changes in flame surface area [1, 2], local and global consumption speeds [3], and flame topology [4, 5]. Interaction between adjacent flames can affect the shape [6, 7], static stability, [8] and dynamic stability [9-13] of a turbulent flame.

Flame-flame interaction events have been modelled using direct numerical simulation (DNS) [14]. Early work focused on the local structure of flames during interaction events and resulted in several key findings. First, flame interaction occurs in stages as different zones of the flame interact, including the

preheat zone, the inner layer, and the oxidation layer. During a flame interaction, the distribution of heat release and species in each zone can change dramatically due to the realignment of species and temperature gradients [15]. Experimental studies have also shown flame-flame interaction leads to increased flame curvature in premixed bluff-body stabilized flames [16]. Second, the high levels of strain and enhanced radical pools, a result of the interacting preheat and reaction layers, result in increased heat-release rate [17] and consumption rate [3]. Finally, flame-flame interaction can result in pocket formation [2, 18], where reactants may diffuse into the products during the interaction and can lead to incomplete combustion [19]. A recent DNS [5, 20] considered the structure and frequency of specific interaction topologies in two interacting rod-stabilized flames. They found that tunnel closures and reactant-pocket formation occur throughout the flame, but high-strain events like product-pocket formation do not occur until far downstream, where the flame is more wrinkled. The wide range of scales over which these events occur poses an obvious challenge for computationally expensive techniques such as DNS and makes experimental investigation a more viable way to statistically characterize these phenomena.

The goal of this study is to investigate the effect of flow interaction on flame-flame interaction. We accomplish this by placing two identical premixed turbulent Bunsen burners 30 mm apart and operating one with a flame and the other without; we apply high-speed laser imaging measurements to study the flame-flame interaction in the resulting flow.

## **2 Experiment Configuration and Methods**

### *2.1 Burner details and experimental configurations*

The experimental facility consists of two identical, premixed high-aspect-ratio Bunsen burners with 100 mm x 10 mm exit planes (Figure 1). Each burner has a lower and an upper section, measuring 178 mm and 160 mm tall, respectively. The lower section contains the inlet for the premixed reactants (natural gas and air), and a ceramic honeycomb flow-straightener. The upper section contains an additional

ceramic honeycomb flow straightener and two perforated plate turbulence generators. These plates have 3.175 mm hole-diameters, 40% open area, and are mounted 30 and 10 mm upstream of the burner exit. The plates are designed to produce a uniform flow with high turbulence at the burner exit [21]. Each burner also contains two pilots, thin pilot flames aligned with the 100 mm edges of the burner exit that anchor the flame and a wider outer pilot that back-support the flames downstream.

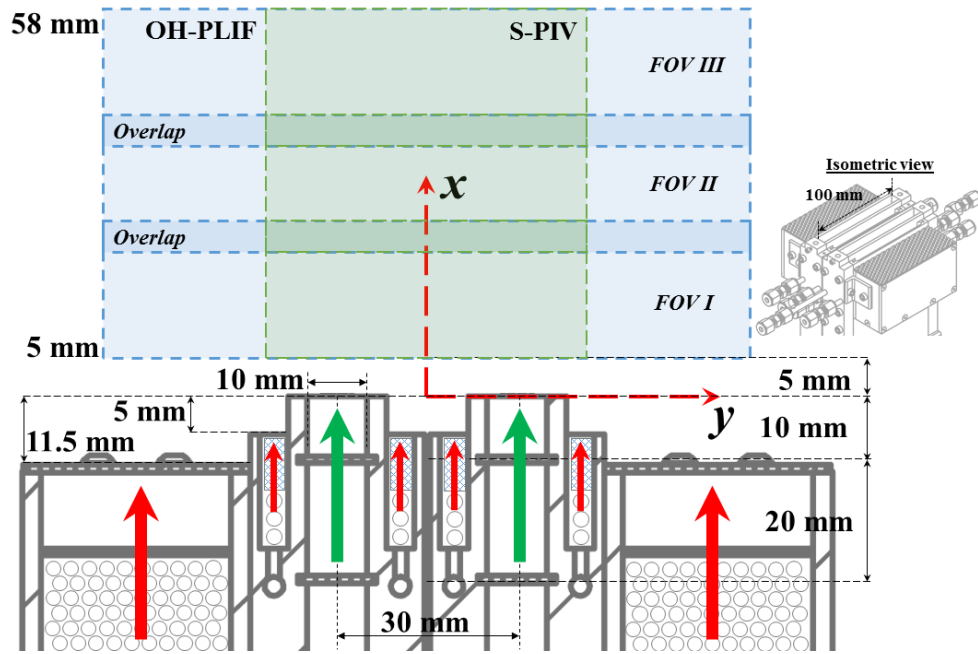


Figure 1: Burner cross-section: larger green arrows represent the main flame flow passage, smaller red arrows and larger red arrows represent the pilot flame flow passage.

This versatile facility can be operated in a variety of modes. In this study, a *flame-flow* configuration is used, where one burner supports a flame and the other flows air at varying velocities. This flame-flow configuration allows us to change the flow interaction between neighboring burners while maintaining a stable flame in the reacting burner. Using this configuration, flames can be subjected to significant flow interaction on one side, while the other flame branch experiences quiescent conditions. This allows for studying flame-flow interaction effects on the inner branch of the left-burner flame, and keeping the boundary conditions on the outer branch of the flame similar to most canonical single burner experiments. Table 1 shows the test matrix for this study. In this table,  $U_{Left}$  and  $U_{Right}$  correspond to the bulk flow

velocities of the reacting- and non-reacting burner, respectively. For all cases in Table 1, the premixed reactants are natural gas and air for main and pilot flames and all the equivalence ratios are kept constant at unity. Additionally, the bulk flow velocities of the thin pilot flames and the outer pilot flames are kept constant at 3 m/s and 4.3 m/s, respectively. The center-to-center distance ( $S$ ) between the burners is 30 mm. For each case, the integral length and velocity scales measured at the reacting burner exit are 2.1 mm and 2.2 m/s, and the corresponding turbulent Reynolds number is 328. The turbulent kinetic energy measured at this location is  $4.4 \text{ m}^2/\text{s}^2$ .

**Table 1: Test matrix for all flames studied**

<i>Case</i>	$U_{Left}$ [m/s]	$U_{Right}$ [m/s]
<i>A</i>	12	20
<i>B</i>	12	25
<i>C</i>	12	30
<i>D</i>	12	35
<i>E</i>	12	40

## 2.2 *Diagnostics method*

### 2.2.1 *OH-PLIF System*

A 10-kHz OH-planar laser induced fluorescence (OH-PLIF) system is used to obtain instantaneous flame front locations in three fields of view (FOV), shown in Figure 1. The maximum power output from the Nd:YAG laser of the system at 10 kHz repetition rate is 53 W, which results in a 0.3 mJ/pulse output from the dye laser. The dye laser output is tuned to the  $Q_1(6)$  line of the  $A^2\Sigma^+ \leftarrow X^2\Pi(1-0)$  band to excite the OH radicals at 282.94 nm. The UV beam is passed through a periscope and a set of three cylindrical lenses to obtain a collimated sheet with an approximate height of 21 mm. A CMOS camera (Photron FASTCAM SA1.1), coupled with an external intensifier (LaVision HS-IRO), a 100 mm f/2.8 UV lens (Cercos) and bandpass interference filter (LaVision Model 1108760) is used to image the OH-signal. The resulting image resolution is 0.1 mm/pixel. A short (100 ns) intensifier gate was used to minimize background luminosity in the images.

### 2.2.2 *S-PIV System*

A high-repetition-rate, dual cavity Nd:YAG laser operating at 532 nm is used, along with a pair of CMOS sensor cameras (Photron FASTCAM SA5) equipped with 100 mm f/2.8 lenses (Tokina Macro) to perform S-PIV measurements. Nikon teleconverters are used on the cameras to accommodate a safe stand-off distance from the burners. Scheimpflug adapters account for the relative angle between the laser sheet and the cameras, and forward-forward scatter mode is implemented. The 532 nm laser beam is passed through a periscope, and a collection of three cylindrical lenses form a collimated sheet with an approximate height of 50 mm. The flowfield is seeded with 0.5-2 micron aluminum oxide particles, and the 532 nm laser-illuminated images are collected at 10 kHz in double-frame mode, with a pulse separation of 14  $\mu$ s. Near-infrared filters and laser line filters are utilized to filter the signal before it is collected on the camera sensor. Vector calculations are performed using DaVis 8.3 from LaVision. Using a multi-pass algorithm, vector-fields are calculated, where the window sizes range from 64x64 to 16x16; for each pass, a 50% overlap is used resulting in an inter-vector distance of 0.48 mm. Vector post-processing is performed with a universal outlier detection scheme with a 3x median filter. Using the uncertainty calculation algorithm in DaVis, a maximum uncertainty of  $\pm 0.46$  m/s is obtained in the shear layer locations. This matches a  $\pm 0.1$  pixel uncertainty of the cross-correlation peak-finding algorithm, which is estimated to be  $\pm 0.43$  m/s.

## 3 Results and discussion

Figure 2 shows the time-averaged vorticity along the inner and outer shear layers of the burner at non-reacting conditions. The locations of mean shear were obtained by identifying the maximum absolute value of the mean vorticity as a function of downstream distance for the inner and outer shear layers, individually. The vorticity is calculated in the first two FOV, where the dotted gray lines indicate the

overlap region between the laser sheets. The time-averaged vorticity differs between the inner and outer shear layers at the burner exit; however, as the vorticity decays with downstream distance, the vorticity in the inner and outer shear layers become similar. These vorticity results, as well as other analyses of the flowfield, indicate that the structure of flowfield differs on either side of the flame near the flame attachment point. As the flow develops downstream, the shear layers merge and the vorticity and turbulence intensity (not shown) become more uniform across the span of the burner.

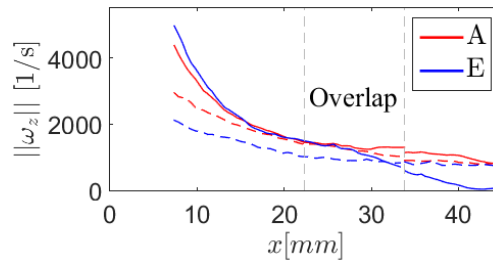


**Figure 2: Mean vorticity along the inner-(solid) and outer-mean shear locations (dashed) for the left burner.**

The presence of the jet on one side of the flame affects the time-averaged progress variable field ( $\bar{c}$ ). The time-averaged progress variable is calculated by averaging binarized instantaneous images of reactants ( $c=0$ ) and products ( $c=1$ ), which are obtained by first applying median and bilateral filtering to the sheet-corrected OH-PLIF images and then thresholding using Otsu's method [22]. Figure 3 shows two examples of  $\bar{c}$  images for flames A and E. The progress variable fields show the flame leaning towards the centerline of the two burners; the bias is greater for flame E than flame A. Horizontal slices of  $\bar{c}$  in Figure 3 at various streamwise locations show this bias more concretely. In this figure, the vertical-dashed line represents the centerline of the reacting burner. The distribution of  $\bar{c}$  near the nozzle exit is symmetric with respect to the burner centerline. However,  $\bar{c}$  distributions further downstream show that the time-averaged flame structure bends towards the centerline of the experiment as a result of enhanced entrainment by the non-reacting burner. The  $\bar{c}$  distribution biases further towards the centerline as the non-reacting jet velocity increases, as a result of increased entrainment. These results imply that in a multi-

nozzle facility, such as the current experiment, statistics that are conditioned on  $\bar{c}$  are dependent on adjacent flow conditions, and canonical single-burner experiment cannot accurately capture these effects.

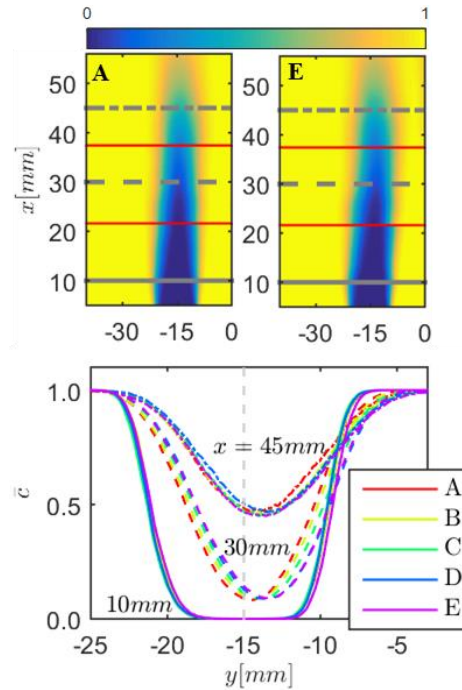


**Figure 3: Stacked progress variables and horizontal slices at various downstream locations. Red lines represent the stitched locations.**

The flow interaction also has an impact on the local characteristics of the flame, including the flame curvature statistics and the frequency and topology of flame interaction events. Figure 4 shows the curvature PDFs for the inner and outer branches of all flames. These PDFs show that the inner branch has more negative curvatures than the outer branch in all cases. Table 2 shows the skewness factors ( $S_i$  and  $S_o$ ) for the inner- and outer-flame branches, respectively. Positive values of  $S_i$  for PDF trends in FOV I indicate that a large number of curvatures are negative, illustrating that the inner-flame branches are more negatively curved than the outer-flame in these flames. This result is similar to that of Worth and Dawson [16] in their study of two interacting bluff-body stabilized flames; the negative curvatures were indicative of more flame cusping events. Studies by Dunstan and co-workers [5, 20] showed that local flame-flame

interactions with negative curvatures are either counter-normal, tunnel-closure, or pocket burn-outs. This suggests that the inner branches of flames in the current study could display these types of interactions.

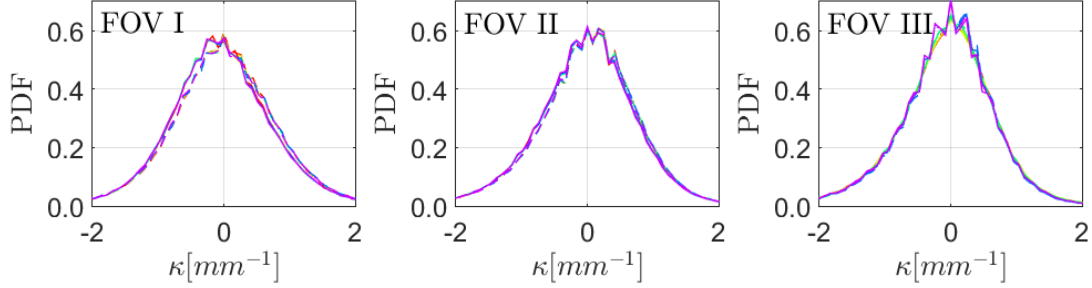


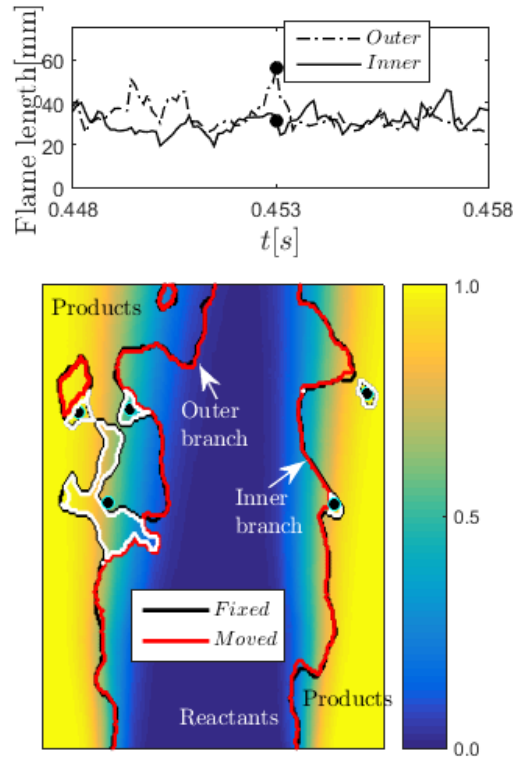
**Figure 4: PDF of flame front curvatures for outer-(dashed) and inner-branches (solid) of the left burner flame.**

**Table 2: Skewness factors for curvature PDFs**

<i>Case</i>	<i>FOV I</i>		<i>FOV II</i>		<i>FOV III</i>	
	$S_i$	$S_o$	$S_i$	$S_o$	$S_i$	$S_o$
<i>A</i>	0.26	-0.02	-0.30	-0.52	-0.93	-0.94
<i>B</i>	0.35	-0.01	-0.34	-0.55	-0.84	-0.88
<i>C</i>	0.36	0.07	-0.31	-0.46	-0.82	-0.91
<i>D</i>	0.31	0.08	-0.33	-0.51	-0.99	-1.12
<i>E</i>	0.38	0.10	-0.29	-0.47	-0.84	-0.97

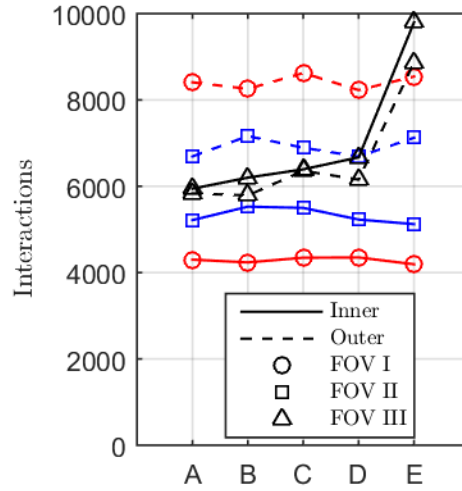
The negative bias in the flame-front curvatures is only observed in the first FOV. Turbulence development further downstream seems to equalize the curvature statistics between the inner and outer flame fronts. The bias of negative curvatures in FOV I is indicative of differences in the shear layer development between the inner and outer shear layers, which affect the flame attachment regions. The similarity of curvature PDFs between the inner and outer branches in FOVs II and III likely reflects the development of the inner and outer shear layers. Additionally, the velocity of the non-reacting jet adjacent to the slot flame does not affect the flame curvature PDFs. These differences in flame curvature PDFs near the flame attachment region have implications for interacting flowfields in multi-nozzle devices. In particular, the flow-interaction effects seem limited to the flame base, whereas the turbulent flow development downstream washes out the effects of flow interaction. This result means that single-nozzle geometries may capture the behavior of flames at further downstream distances, but possibly not near the flame-attachment region.

Changes in the curvature PDFs indicate that the instantaneous topology of the flame is different on the inner and outer branches, and one reason may be differences in local flame interaction [5, 16, 20]. Flame interaction events are identified using a non-rigid image registration technique (described as Automatic Feature Extraction in [5, 20]), which compares a pair of high-speed OH-PLIF images to map the transformations in the flame front due to local convection of the flame. For each data set, 9998 pairs of consecutive OH-PLIF images are processed to obtain a time series of flame-flame interactions, which register as regions of topological change on the flame front over a time step  $\Delta t$ . The centroids of these regions are calculated to identify the location of each interaction. Figure 5 (bottom) shows examples of identified interactions with black markers representing the centroids of these interaction regions. The centroids are used to identify the location of interaction events and time-averaged progress variables extracted at the centroid locations are called flame interaction conditioned progress variables. Curvatures are extracted from ‘fixed’ flame edge pixels that are nearest to flame interaction centroids and are called flame interaction conditioned curvatures. These curvature values give a general sense of wrinkling of the flame before the occurrence of an interaction event.



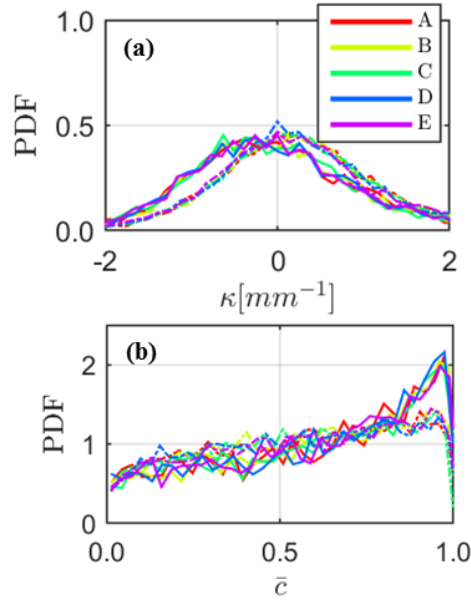
**Figure 5: Instantaneous flame branch lengths (top) and flame edges and flame-flame interactions (bottom) for case E.**

Figure 6 shows the number of flame-flame interactions occurring in the inner and outer branches of the flames. In FOV I, the number of interactions in the inner branch is smaller than in the outer branch; this finding aligns with the curvature PDF results, where the inner branch displays more negative curvatures. In FOV II, the differences are smaller, which is reflected in the curvature PDF results as well. In FOV III, the number of interactions occurring in the inner and outer branches are similar, likely due to shear layer merging and the proximity of the two branches at the tip. Analysis of the flame edge movies shows that a majority of interactions occurring in FOV III are pocket formations. For flame E, the number of interactions is quite large as compared with the rest of the test cases. The flame-edge movie for this case shows that large numbers of pockets are formed in this region, and some pockets break into several smaller pockets that eventually burn out. The enhanced interactions in FOV III of flame E are likely driven by the interaction with the high-velocity jet adjacent to the flame, which entrains the tip of the flame at these high speeds.



**Figure 6: Number of flame-flame interaction events on the inner- and outer-branches of the left burner flame.**

Using the centroid of the flame-flame interactions, flame curvatures and time-averaged progress variables can be conditionally extracted to identify topological features of the interaction sites. Figure 7(a) and (b) show the PDFs of these conditional flame curvatures and  $\bar{c}$ , respectively. The curvature PDF shows that the inner branch interactions tend to have more negative curvatures than the outer branch interactions. The mean interaction conditioned curvatures for the outer flame branch are more positive than that for the inner flame branch, which are consistent with the observations in Figure 7(a).



**Figure 7: (a) PDF of flame interaction conditioned curvatures, (b) PDF of flame interaction conditioned ( $\bar{c}$ ) in FOV I for the inner- (solid) and outer- branches (dashed).**

Figure 7(b) shows the PDF of the conditional  $\bar{c}$  values at the locations of flame-flame interactions. This PDF shows the impact of entrainment of the flame by the adjacent jet; a high number of interactions occur in  $\bar{c}=0.9-1$  locations for the inner flame branch but not for the outer. This entrainment of the flame is also evident in Figure 3, where the minima in  $\bar{c}$  shift away from the centerline of left burner. The differences between the inner and outer branches in the conditional  $\bar{c}$  PDF suggest that conditional statistics can significantly vary in the near-fields of interacting versus non-interacting flames.

Inspection of flame-edge movies shows that the size of the interaction events are different in the inner and outer branches. The inner branch interactions, on the whole, have smaller length scales as compared to the outer branch interactions. Figure 5 shows an example of an instantaneous interaction occurring in both the inner and outer branches of the flame. In the bottom part of this figure, the white edges represent the flame-front reduction regions in a time step  $\Delta t$  from the image registration technique. The red edge (fixed) represents the flame at the first time and the black edge (moved) represents the flame at the next time step. A time series of the inner and outer flame-branch lengths for this FOV is also shown

in the top part of this figure, where black dots on each flame-branch length time series represent the time instant of the flame edges shown in bottom part of the same figure. The flame-branch lengths for each branch are calculated by summing the arc length of the instantaneous flame-branch edge, including pockets. Large length-scale interactions on the outer branch have a bigger impact on the global flame length, or in a three-dimensional sense, the flame area. The inner branch, on the other hand, experiences small length-scale interactions, and hence, the global flame length variations are usually smaller. Significant reactant pocket formation and consumption is also observed due to the large length-scale interactions in the outer branch. From our observations of the instantaneous velocity fields, it is likely that large-scale vortices are driving these large length scale interactions in the outer branch of the flames. The large-scale interactions illustrate the importance of understanding large-scale fluid motions and the impact that flow interaction has on the hydrodynamic stability characteristics of the flow and flame behavior.

#### **4 Conclusions**

High-speed laser imaging measurements were used to statistically characterize the effect of increasing mean shear on the local and global topology of flame-flame interaction events in a turbulent premixed slot flame. The presence of a high mean-shear flow adjacent to one branch of the flame causes a bending of the time-averaged flame structure towards the experiment centerline. In addition, the inner branch of the flame shows a negative bias in flame curvatures compared with the outer branch near the flame attachment region, while in the far-field regions, this phenomena is not observed. In the near-attachment region, a larger number of local flame-flame interactions occur in the outer branches of the flame compared with the inner branches. Based on velocity-field observations, large-scale vortical motions likely drive these flame area consumptions in the outer branches. This work highlights the importance of considering the boundary condition that the adjacent flow places on a flame. This adjacent flow alters the time-averaged progress variable distribution, the curvature statistics, and the local flame interaction statistics. These results suggest that interaction between adjacent flows is an important

consideration in predicting the local and global behavior of flames, and single-flame experiments may not capture the richness of flame dynamics present in combustion systems with multiple flows.

### **Acknowledgements**

This work was supported by the Air Force Office of Scientific Research under Grants FA9550-16-1-0075 and FA9550-16-1-0044 with program manager Dr. Chiping Li. The authors acknowledge Dr. Campbell Carter (AFRL) for lending equipment and advice for these experiments.

## References

- [1] N. Fogla, F. Creta, M. Matalon, *Combust. Flame* 162 (7) (2015) 2758-2777.
- [2] J.H. Chen, T. Echehki, W. Kollmann, *Combust. Flame* 116 (1) (1999) 15-48.
- [3] H.G. Im, J.H. Chen, *Combust. and Flame*, 131 (3) (2002) 246-258.
- [4] R. Griffiths, J.H. Chen, H. Kolla, R. Cant, W. Kollmann, *Proc. Combust. Inst.*, 35 (2) (2015) 1341-1348.
- [5] T. Dunstan, N. Swaminathan, K. Bray, N. Kingsbury, *Combust. Sci. Technol.* 185 (1) (2013) 134-159.
- [6] N.A. Worth, J.R. Dawson, *Meas. Sci. and Technol.* 24 (2) (2012) 024013.
- [7] J. Samarasinghe, S. Peluso, M. Szedlmayer, A. De Rosa, B. Quay, D. Santavicca, *J. Eng. Gas Turbines Power* 135 (10) (2013) 101503.
- [8] J. Kariuki, N.A. Worth, J.R. Dawson, E. Mastorakos, *AIAA ASM paper (AIAA 2013-0692)* (2013).
- [9] U. Hegde, D. Reuter, B. Daniel, B. Zinn, *Combust. Sci. Technol.* 55(4-6) (1987) 125-138.
- [10] D. Reuter, U. Hegde, B. Zinn, *J. Prop. and Power*, 6 (6) (1990) 680-685.
- [11] D. Fanaca, P.R. Alemela, F. Ettner, C. Hirsch, T. Sattelmayer, B. Schuermans, *ASME Turbo Expo (GT2008-50781)*, pp. 565-573 (2008) 565-573.
- [12] J.R. Dawson, N.A. Worth, *Combust. Flame* 161 (10) (2014) 2565-2578.
- [13] M. Aguilar, M. Malanoski, G. Adhitya, B. Emerson, V. Acharya, D. Noble, T. Lieuwen, *J. Eng. Gas Turbines Power* 137(9) (2015) 091507.
- [14] J. Park, T. Echehki, *Combust. Flame* 159 (2) (2012) 609-620.
- [15] T. Echehki, J.H. Chen, I. Gran, *Proc. Combust. Inst.* 26(1) (1996) 855-863.
- [16] N.A. Worth, J.R. Dawson, *Combust. Flame* 159 (3) (2012) 1109-1126.
- [17] B. Ranganath, T. Echehki, *Int. J. Heat Mass Transfer* 49 (25) (2006) 5075-5080.
- [18] W. Kollmann, J.H. Chen, *Proc. Combust. Inst.* 27(1) (1998) 927-934.
- [19] C. Sun, C. Law, *Proc. Combust. Inst.* 27(1) (1998) 963-970.
- [20] T. Dunstan, N. Swaminathan, K. Bray, N. Kingsbury, *Combust. Sci. Technol.* 185(6) (2013) 874-897.
- [21] P.E. Roach, *Int. J. Heat Fluid Flow* 8 (2) (1987) 82-92.
- [22] R.C. Gonzalez, R.E. Woods, *Digital Image Processing*, Prentice Hall, Upper Saddle River, NJ (2002).

## List of Figures

Figure 1: Burner cross-section: larger green arrows represent the main flame flow passage, smaller red arrows and larger red arrows represent the pilot flame flow passage.

Figure 2: Mean vorticity along the inner-(solid) and outer-mean shear locations (dashed) for the left burner.

Figure 3: Stitched progress variables and horizontal slices at various downstream locations. Red lines represent the stitched locations.

Figure 4: PDF of flame front curvatures for outer- (dashed) and inner-branches (solid) of the left burner flame.

Figure 5: Instantaneous flame branch lengths (top) and flame edges and flame-flame interactions (bottom) for case E.

Figure 6: Number of flame-flame interaction events on the inner- and outer-branches of the left burner flame.

Figure 7: (a) PDF of flame interaction conditioned curvatures, (b) PDF of flame interaction conditioned ( $\bar{c}$ ) in FOV I for the inner- (solid) and outer-branches (dashed).